

LETTER • OPEN ACCESS

## Global fluid simulation of plasma turbulence in a stellarator with an island divertor

To cite this article: A.J. Coelho *et al* 2022 *Nucl. Fusion* **62** 074004

View the [article online](#) for updates and enhancements.

### You may also like

- [Direct measurements of counter-streaming flows in a low-shear stellarator magnetic island topology](#)  
V. Perseo, F. Effenberg, D. Gradic et al.
- [Overview of the results from divertor experiments with attached and detached plasmas at Wendelstein 7-X and their implications for steady-state operation](#)  
M. Jakubowski, M. Endler, Y. Feng et al.
- [First demonstration of radiative power exhaust with impurity seeding in the island divertor at Wendelstein 7-X](#)  
F. Effenberg, S. Brezinsek, Y. Feng et al.

## Letter

# Global fluid simulation of plasma turbulence in a stellarator with an island divertor

A.J. Coelho\* , J. Loizu, P. Ricci and M. Giacomin 

École Polytechnique Fédérale de Lausanne (EPFL), Swiss Plasma Center (SPC), CH-1015 Lausanne, Switzerland

E-mail: [antonio.coelho@epfl.ch](mailto:antonio.coelho@epfl.ch)

Received 26 January 2022, revised 28 March 2022

Accepted for publication 27 April 2022

Published 17 May 2022



CrossMark

## Abstract

Results of a three-dimensional, flux-driven, electrostatic, global, two-fluid turbulence simulation for a five-field period stellarator with an island divertor are presented. The numerical simulation is carried out with the GBS code, recently extended to simulate plasma turbulence in non-axisymmetric magnetic equilibria. The vacuum magnetic field used in the simulation is generated with the theory of Dommaschk potentials, and describes a configuration with a central region of nested flux surfaces, surrounded by a chain of magnetic islands, similar to the diverted configurations of W7-X. The heat outflowing from the core reaches the island region and is transported along the magnetic islands, striking the vessel walls, which correspond to the boundary of the simulation domain. The radial transport of particles and heat is found to be mainly driven by a field-aligned coherent mode with poloidal number  $m = 4$ . The analysis of this mode, based on non-local linear theory considerations, shows its ballooning nature. In contrast to tokamak simulations and experiments, where blobs often contribute to transport, we do not observe the presence of intermittent transport events.

Keywords: stellarators, turbulence fluid simulation, GBS

(Some figures may appear in colour only in the online journal)

## 1. Introduction

In the recent years, the magnetic fusion community has increasingly focussed its attention on how particles and heat can be exhausted without damaging the plasma-facing materials, while simultaneously preserving good core performance.

Most tokamaks are currently operated in an axisymmetric single-null diverted configuration, consisting of a central region of closed field lines, surrounded by the scrape-off layer (SOL), a region of open field lines that are diverted by using external coils and end up on the solid surfaces of the divertor plates at a certain distance from the core. The single-null configuration will be adopted by ITER [1], while alternative configurations such as the snowflake or the double-null are being explored for DEMO [2]. In addition, 3D perturbations might be used to mitigate and control edge localized modes, affecting the heat pattern deposition and possibly the boundary turbulence [3, 4]. As for stellarators, diverted solutions also exist. In W7-X the so-called *island divertor* configuration is used [5],

\* Author to whom any correspondence should be addressed.



Original content from this work may be used under the terms of the [Creative Commons Attribution 4.0 licence](https://creativecommons.org/licenses/by/4.0/). Any further distribution of this work must maintain attribution to the author(s) and the title of the work, journal citation and DOI.

where a chain of magnetic islands surrounds the closed field-line region, and the heat outflowing from the core is diverted along the field lines of the islands that strike the plasma-facing components. Other possible exhaust solutions used in stellarators include the ergodic divertor employed in LHD [6] and the non-resonant divertor envisaged for HSX [7].

The interplay between the plasma fluxes from the core, the cross-field transport across the magnetic field lines and the losses to the walls determine the peak heat loads at the vessel targets [8]. While boundary turbulence has been thoroughly characterized experimentally in tokamaks [9], similar investigations are still in their infancy in stellarators. In addition to the measurements carried out in small, low-temperature plasma stellarators such as TJ-K [10–12], experimental measurements in the edge of W7-X are recent [13–15]. These have shown significant differences with respect to tokamaks: field-aligned structures (dubbed filaments) are observed to be essentially bound to their flux surface, covering very small radial distances due to their slow radial velocity of the order of  $100 \text{ m s}^{-1}$  [13, 14], while their poloidal velocities are of the order of a few  $\text{km s}^{-1}$  [15]. Similar observations are reported in the edge of LHD [16, 17]. On the other hand, typical tokamak measurements show blobs generated near the separatrix that travel ballistically across the SOL and provide an important contribution to the global perpendicular transport, with radial velocities of the order of a few  $\text{km s}^{-1}$  [18, 19]. In W7-X, the fluctuations are approximately normally distributed [15], hinting that the turbulent structures are the result of fluctuations that have a local origin rather than being advected from a different radial position, in agreement with their small radial velocity [14]. While a broad-band turbulent spectrum in the range 1–10 kHz is observed in stellarators as in tokamaks [13, 15], quasi-coherent modes with 10–50 kHz and small poloidal wave-numbers (corresponding to a wavelength of approximately 30 cm), propagating both in the ion and electron diamagnetic drift directions, are also observed in W7-X [13].

Similarly to the experimental investigations, the simulation of plasma dynamics in the stellarator boundary is still at a very early stage. The fluid code BOUT++ simulated seeded plasma filaments in a slab geometry that emulates the radially varying connection lengths of W7-X [20] and it was recently extended to simulate non-axisymmetric magnetic fields such as a low-field-period rotating ellipse [21].

In this letter we present results of the first global, two-fluid, flux-driven simulation of a stellarator with an island divertor. The simulation is performed with the GBS code, which has been used in the past decade to simulate the tokamak boundary [22–28], and it is here extended to non-axisymmetric magnetic fields. GBS solves the drift-reduced Braginskii equations [29], valid in the high collisionality regime, which is often justified in the plasma boundary of magnetic fusion devices as well as in the core of low-temperature devices (e.g., TJ-K [30]). All quantities are evolved in time without separation between equilibrium and fluctuating parts. We consider here the electrostatic limit, we apply the Boussinesq approximation [22], and we neglect gyroviscous terms as well as the coupling to the neutral dynamics, although these are implemented in the most

recent version of the GBS code for tokamak simulations [23]. Within these approximations, the drift-reduced model evolved by GBS is:

$$\frac{\partial n}{\partial t} = -\frac{\rho_*^{-1}}{B} [\Phi, n] - \nabla_{\parallel} (nV_{\parallel e}) + \frac{2}{B} [C(p_e) - nC(\Phi)] + D_n \nabla_{\perp}^2 n + D_n^{\parallel} \nabla_{\parallel}^2 n + S_n \quad (1)$$

$$\begin{aligned} \frac{\partial T_e}{\partial t} = & -\frac{\rho_*^{-1}}{B} [\Phi, T_e] - V_{\parallel e} \nabla_{\parallel} T_e \\ & + \frac{4T_e}{3B} \left[ \frac{C(p_e)}{n} + \frac{5}{2} C(T_e) - C(\Phi) \right] \\ & + \frac{2T_e}{3n} [0.71 \nabla_{\parallel} j_{\parallel} - n \nabla_{\parallel} V_{\parallel e}] \\ & + D_{T_e} \nabla_{\perp}^2 T_e + \chi_{\parallel e} \nabla_{\parallel}^2 T_e + S_{T_e} \end{aligned} \quad (2)$$

$$\begin{aligned} \frac{\partial T_i}{\partial t} = & -\frac{\rho_*^{-1}}{B} [\Phi, T_i] - V_{\parallel i} \nabla_{\parallel} T_i \\ & + \frac{4T_i}{3B} \left[ \frac{C(p_e)}{n} - \frac{5}{2} \tau C(T_i) - C(\Phi) \right] \\ & + \frac{2T_i}{3n} [\nabla_{\parallel} j_{\parallel} - n \nabla_{\parallel} V_{\parallel i}] + D_{T_i} \nabla_{\perp}^2 T_i \\ & + \chi_{\parallel i} \nabla_{\parallel}^2 T_i + S_{T_i} \end{aligned} \quad (3)$$

$$\begin{aligned} \frac{\partial V_{\parallel e}}{\partial t} = & -\frac{\rho_*^{-1}}{B} [\Phi, V_{\parallel e}] - V_{\parallel e} \nabla_{\parallel} V_{\parallel e} \\ & + \frac{m_i}{m_e} \left[ \nu j_{\parallel} + \nabla_{\parallel} \Phi - \frac{\nabla_{\parallel} p_e}{n} - 0.71 \nabla_{\parallel} T_e \right] \\ & + \eta_{0e} \nabla_{\parallel}^2 V_{\parallel e} + D_{V_{\parallel e}} \nabla_{\perp}^2 V_{\parallel e} \end{aligned} \quad (4)$$

$$\begin{aligned} \frac{\partial V_{\parallel i}}{\partial t} = & -\frac{\rho_*^{-1}}{B} [\Phi, V_{\parallel i}] - V_{\parallel i} \nabla_{\parallel} V_{\parallel i} - \frac{1}{n} \nabla_{\parallel} (p_e + \tau p_i) \\ & + \eta_{0i} \nabla_{\parallel}^2 V_{\parallel i} + D_{V_{\parallel i}} \nabla_{\perp}^2 V_{\parallel i} \end{aligned} \quad (5)$$

$$\begin{aligned} \frac{\partial \omega}{\partial t} = & -\frac{\rho_*^{-1}}{B} [\Phi, \omega] - V_{\parallel e} \nabla_{\parallel} \omega + \frac{B^2}{n} \nabla_{\parallel} j_{\parallel} \\ & + \frac{2B}{n} C(p_e + \tau p_i) + D_{\omega} \nabla_{\perp}^2 \omega + D_{\omega}^{\parallel} \nabla_{\parallel}^2 \omega \end{aligned} \quad (6)$$

$$\nabla_{\perp}^2 \Phi = \omega - \tau \nabla_{\perp}^2 T_i \quad (7)$$

In equations (1)–(7), all quantities are normalized to reference values: density  $n$ , electron temperature  $T_e$  and ion temperature  $T_i$  are normalized to  $n_0$ ,  $T_{e0}$  and  $T_{i0}$ ; electron parallel velocity  $V_{\parallel e}$  and ion parallel velocity  $V_{\parallel i}$  are both normalized to the sound speed  $c_{s0} = \sqrt{T_{e0}/m_i}$ ; vorticity  $\omega$  and the electrostatic potential  $\Phi$  are normalized to  $T_{e0}/(e\rho_{s0}^2)$  and  $T_{e0}/e$ ; time is normalized to  $R_0/c_{s0}$ , where  $R_0$  is the machine major radius; and perpendicular and parallel lengths are normalized to the ion sonic Larmor radius,  $\rho_{s0} = \sqrt{T_{e0}m_i}/(eB_0)$ , and  $R_0$ , respectively. The normalized parallel current is  $j_{\parallel} = n(V_{\parallel i} - V_{\parallel e})$  and  $B$  is the magnetic field normalized to the magnitude of the field on axis,  $B_0$ .

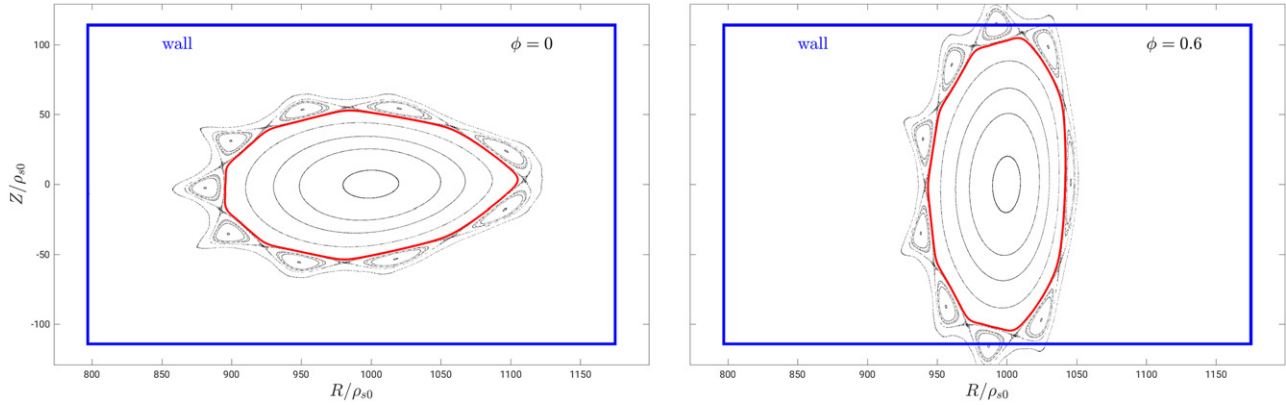


**Figure 1.** Poincaré plot of the magnetic field used in this work on two poloidal planes at different toroidal angles. The boundary of the simulation domain is represented in blue.

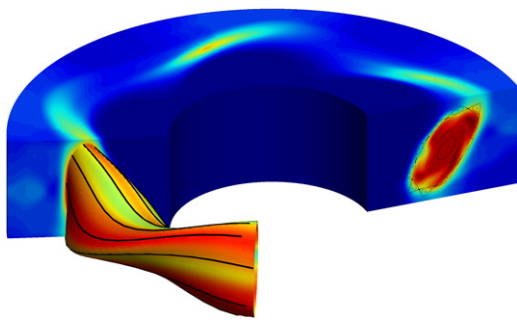


**Figure 2.** Three-dimensional snapshot of plasma density, representing the geometry of the simulation considered here. The surface depicted corresponds to the LCFS and a field line (black line) is superimposed.

The dimensionless parameters appearing in the equations are the normalized ion sonic Larmor radius  $\rho_* = \rho_{s0}/R_0$ , the normalized electron and ion parallel diffusivities,  $\chi_{\parallel e}$  and  $\chi_{\parallel i}$ , considered here as constants, the ion to electron temperature ratio  $\tau = T_{i0}/T_{e0}$ , the normalized electron and ion viscosities,  $\eta_{0e}$  and  $\eta_{0i}$ , which we also set to constant values, and the normalized Spitzer resistivity  $\nu = \nu_0 T_e^{3/2}$  with  $\nu_0$  given in [26]. Small numerical diffusion terms such as  $D_n \nabla_{\perp}^2 n$  and  $D_n^{\parallel} \nabla_{\parallel}^2 n$  (and similar for the other fields) are introduced to improve the numerical stability of the code and the simulation results show that they lead to significantly lower perpendicular transport than turbulence. The terms  $\mathcal{S}_n$ ,  $\mathcal{S}_{T_e}$  and  $\mathcal{S}_{T_i}$  denote the sources of density, electron and ion temperature, respectively. Magnetic pre-sheath boundary conditions, described in [31, 32], are applied to all quantities at the end of the field lines intersecting the walls, except for the density and vorticity, that satisfy, respectively,  $\partial_s n = 0$  and  $\omega = 0$ , where  $s$  is the direction normal to the wall.

The normalized geometrical operators appearing in equations (1)–(7) are the parallel gradient  $\nabla_{\parallel} u = \mathbf{b} \cdot \nabla u$ , the Poisson brackets  $[\Phi, u] = \mathbf{b} \cdot [\nabla \Phi \times \nabla u]$ , the curvature operator  $C(u) = (B/2) [\nabla \times (\mathbf{b}/B)] \cdot \nabla u$ , the parallel Laplacian  $\nabla_{\parallel}^2 u = \mathbf{b} \cdot \nabla (\mathbf{b} \cdot \nabla u)$  and the perpendicular Laplacian  $\nabla_{\perp}^2 u = \nabla \cdot [(\mathbf{b} \times \nabla u) \times \mathbf{b}]$ . While these operators are not toroidally symmetric in contrast to tokamak

simulations, their implementation is straightforward in GBS thanks to the versatility of its non field-aligned. For their numerical implementation, we expand the geometrical operators in the following small parameters: the ratio between the poloidal components and the norm of the magnetic field,  $\delta = B_R/B \sim B_Z/B$ ; the normalized mirror ratio,  $\Delta = (B_{\max} - B_{\min})/\bar{B}$ , where  $\bar{B}$  is the averaged value of  $B$  along the toroidal direction and  $(B_{\max} - B_{\min})$  is the ripple amplitude; and the ratio between perpendicular and parallel turbulence length scales,  $\sigma = l_{\perp}/l_{\parallel}$ . We then retain only the leading order terms in these expansion parameters. For the stellarator configuration considered in this work  $\delta \sim 0.1$ ,  $\Delta \lesssim 0.1$  and *a posteriori* we verify that  $\sigma \sim 0.01$ , confirming the validity of the expansion.

The physical model in equations (1)–(7) is discretized in a cylindrical grid  $(R, \phi, Z)$ , with  $R$  the radial coordinate,  $\phi$  the toroidal angle and  $Z$  the vertical coordinate. The simulation domain is a torus of radius  $R_0$  with a rectangular cross-section of size  $L_R \times L_Z$ . Equations (1)–(6) are advanced in time with an explicit Runge–Kutta fourth-order scheme, while spatial derivatives are computed with a fourth-order finite difference scheme [26, 33].

For the present study we exploit the properties of Dommasck potentials [34] to analytically construct a five-field period stellarator-symmetric vacuum field with a 5/9 chain of islands surrounding a volume of nested magnetic surfaces, which consist essentially of rotating ellipses without torsion. The magnetic shear is very small with the rotational transform varying from 0.500 at the magnetic axis and 0.555 at the last closed flux surface (LCFS). Since the LCFS is not well defined in a stellarator, we consider it as being a surface very close to the island chain (red surface in figure 1). The lengths  $L_R$  and  $L_Z$  are adjusted such that the islands strike the top and bottom of the simulation box, as can be seen in figure 1. In such configuration, heat and particles outflowing from the core reach the island region and are transported along the magnetic field of the islands, eventually striking the top and bottom walls at specific toroidal locations.

The simulation presented here is started from a noisy initial state and, after a transient, reaches a quasi-steady state, where sources, parallel and perpendicular transport and losses

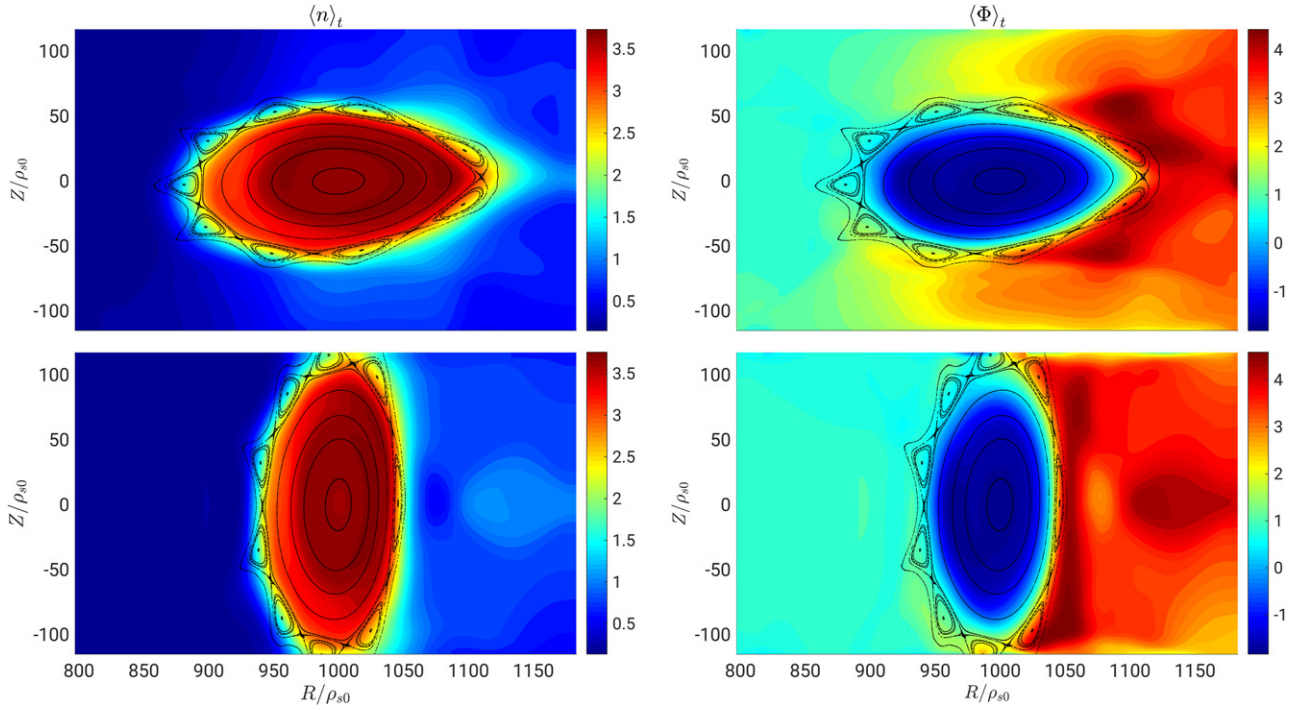


**Figure 3.** Equilibrium profiles of density (left) and electrostatic potential (right), obtained by time-averaging the simulation results. Top and bottom correspond to the toroidal planes  $\phi = 0$  and  $\phi = 0.6$ , respectively.

at vessel balance each other. Therefore, the fluctuating part of the fields is not separated from the equilibrium part in GBS. We focus our discussion on the results of a simulation that uses the following parameters:  $\rho_*^{-1} = 1000$ ,  $\nu_0 = 0.1$ ,  $\tau = 1$ ,  $\chi_{||e,i} = \eta_{0e,i} = 1.0$ ,  $D_n = D_{Te} = D_{Ti} = D_{V||e} = D_{V||i} = D_\omega = 10$ ,  $D_n^|| = D_\omega^|| = 1$ ,  $L_R = 380\rho_{s0}$ ,  $L_Z = 230\rho_{s0}$ , a grid resolution of  $N_R \times N_Z \times N_\phi = 200 \times 120 \times 200$  points and a time-step of  $2.9 \times 10^{-6}R_0/c_{s0}$ . A convergence test to assess the accuracy of the simulation was made. In particular we considered a simulation with grid  $N_R \times N_Z \times N_\phi = 250 \times 150 \times 200$  and another simulation with grid  $N_R \times N_Z \times N_\phi = 250 \times 150 \times 250$ , which is at the limit of our computational capabilities. In both cases we verified that the dynamics of the simulation is similar to the one presented here. The sources for density and temperature,  $S_n = S_{Te} = S_{Ti}$ , are localized around a magnetic surface near the LCFS. In figure 2, a global overview of the simulation geometry is shown with a snapshot of density once the quasi-steady state is reached. Particles are mostly exhausted where field lines strike the vessel, which is revealed by the high plasma density regions appearing on the top wall.

In figure 3 the equilibrium (i.e., time-averaged) profiles of density and potential are shown at two different toroidal locations. We observe that the plasma is well confined inside the LCFS, and that the electrostatic potential is negative in the core and positive in the edge. The radial electric field is therefore negative, which corresponds to the ion-root regime, expected as well in the neoclassical high-collisional regime [35].

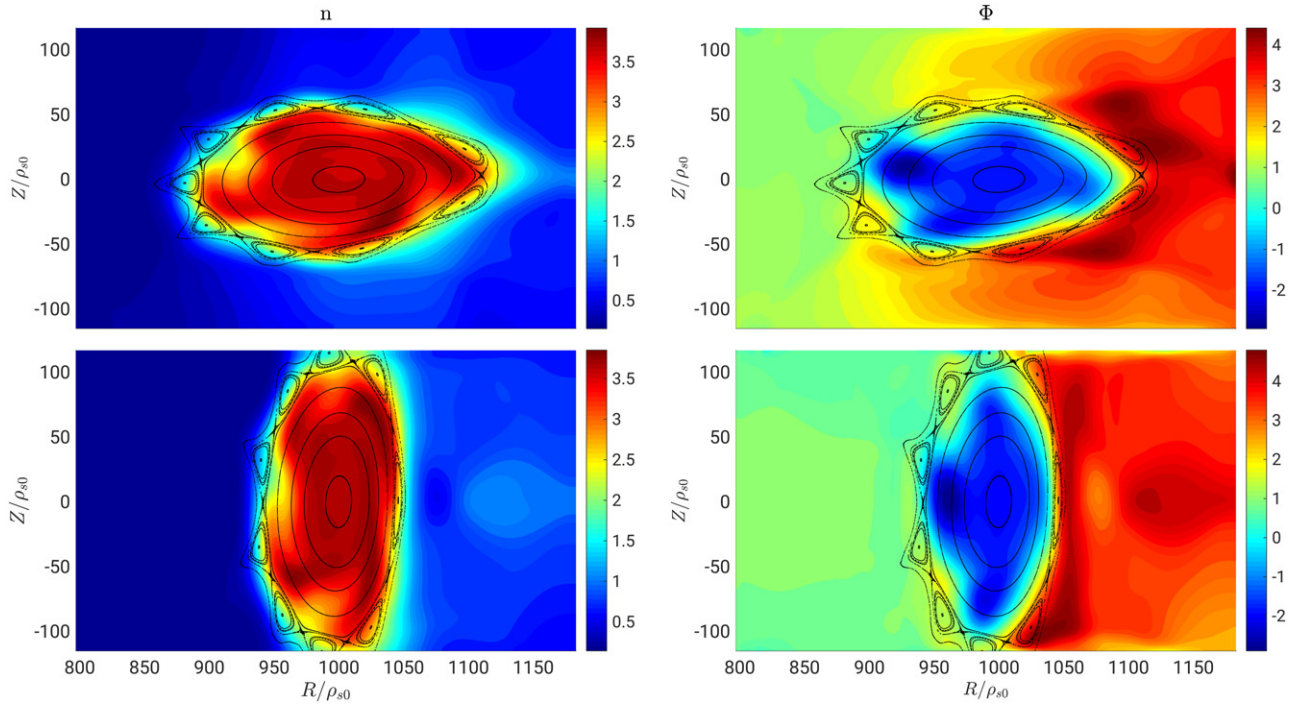
Snapshots of density and electrostatic potential in the quasi-steady state at two different toroidal angles are shown in

figure 4. A mode with poloidal mode number  $m = 4$  (corresponding to  $k_y\rho_{s0} \approx 0.04$ , where  $y$  is the binormal direction, being  $x$  the radial and  $z$  the parallel coordinates) and toroidal mode number  $n = 5$  dominates the global dynamics of the system. The mode is coherent and rotates in the ion diamagnetic direction. Furthermore, the mode is field-aligned, as can be seen in figure 2, where a field line has been traced for several toroidal transits on the LCFS and is shown with a black line. No broad-band turbulence nor blobs are observed, highly contrasting with typical tokamak boundary simulations [36, 37]. The presence of a coherent dominant mode is a robust feature of the simulation. In fact, an  $m = 4$  mode appears in other simulations performed with lower and higher strength of the plasma and temperature sources, and also in simulations with larger sizes,  $\rho_*^{-1} = 1500, 2000$  (not shown). An analysis of Ohm's law (4) shows that the electrostatic approximation for the dominant mode is valid for  $\beta \ll 0.2\%$ .

An analysis on the balance of the density equation shows that approximately 80% of the radial transport of particles across the LCFS is due to the time-averaged fluctuating  $E \times B$ -flux,

$$\Gamma_{E \times B}^x = \left\langle \tilde{n} \tilde{V}_{E \times B}^x \right\rangle_t = - \left\langle \frac{\tilde{n}}{B} (\nabla \tilde{\Phi} \times \mathbf{b})_x \right\rangle_t, \quad (8)$$

where we denote with tilde fluctuating quantities and  $\langle \cdot \rangle_t$  time averages (i.e.,  $n = \tilde{n} + \langle n \rangle_t$ ). The largest contribution to this flux is given by the  $m = 4$  mode. Indeed, we have verified a good agreement between the flux of particles evaluated numerically by using equation (8), and the time-averaged  $E \times B$ -flux due to a single coherent mode,



**Figure 4.** Snapshot of density,  $n$  (left) and electrostatic potential,  $\Phi$  (right), in the quasi-steady state. Top and bottom correspond to the toroidal planes  $\phi = 0$  and  $\phi = 0.6$ , respectively.

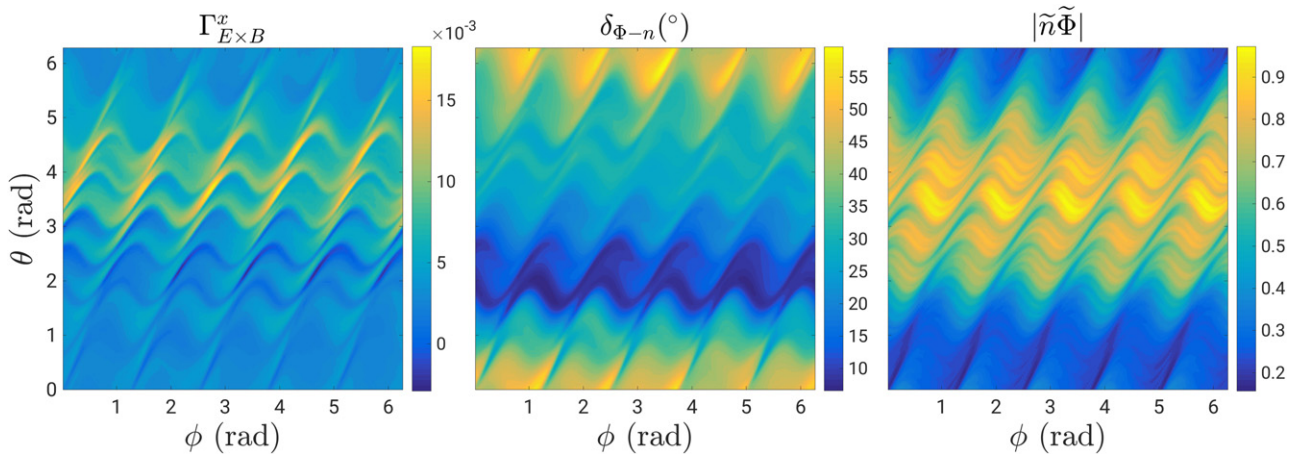


**Figure 5.** Time-averaged fluctuating  $E \times B$  radial flux on the LCFS evaluated according to equation (8) (left panel); phase-difference between potential and density,  $\delta_{\Phi-n}$  (middle panel); fluctuations' amplitude (right panel); as evaluated from the GBS simulation.  $\theta = 0$  corresponds to the outboard midplane.

$$\Gamma^c = \frac{k_y}{2B} |\tilde{n}\tilde{\Phi}| \sin(\delta_{\Phi-n}), \quad (9)$$

where  $\delta_{\Phi-n}$  is the phase-difference between potential and density obtained from the correlation between them, being the fluctuation amplitudes and phase-difference from the simulation results. In figure 5 we show the  $E \times B$ -flux evaluated using equation (8) on the unfolded LCFS (left panel of figure 5), where it is seen that the flux peaks on the stellarator high-field side ( $\theta = 0$  corresponding to the outboard midplane). This is due to the fact that the amplitude of the fluctuations is larger at  $\theta = \pi$  (right panel of figure 5), overcoming the phase-difference term, which is larger on the low-field side (middle panel of figure 5).

We use a non-local linear theory in order to investigate the properties of the coherent mode dominating the simulation. Namely, we linearize GBS equations, equations (1)–(7), by assuming that all quantities vary as

$$u(x, \theta, \phi) = u_0(x) + \tilde{u}(x)e^{\gamma t + i(m\theta - n\phi)}, \quad (10)$$

where  $x$  ranges from 0 at the magnetic axis to 1 at the LCFS,  $u_0$  is the background profile obtained from the GBS simulation by time and flux surface averaging,  $m$  and  $n$  are the poloidal and toroidal mode numbers and  $\gamma$  is the growth-rate of the mode. Note that the mode  $\tilde{u}$  depends on  $x$ , in agreement with the non-local nature of the mode dominating the simulation. In the linearized system of equations, we simplify the magnetic

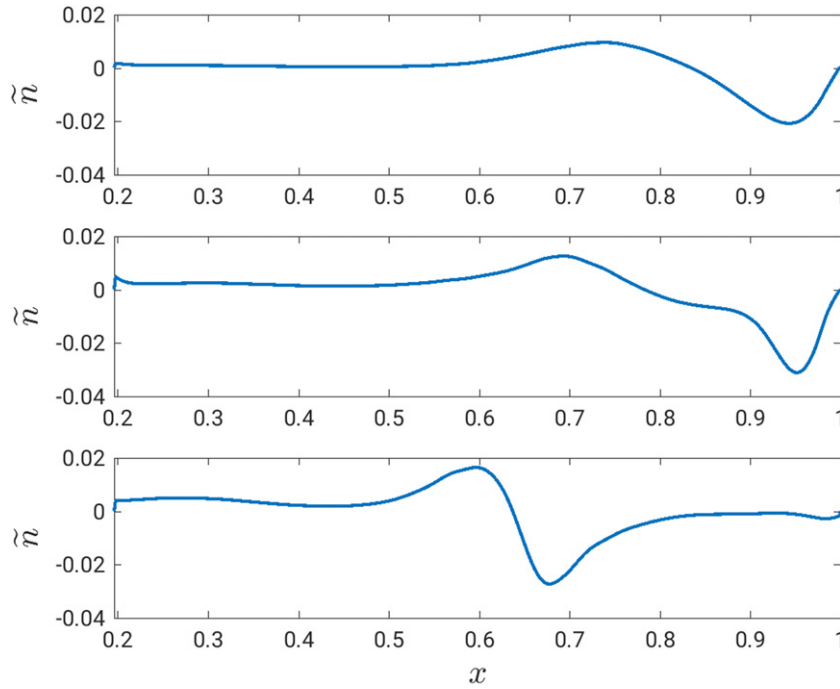


**Figure 6.** Density eigenmodes resulting from the linear theory with  $m = 4$  and  $n = 5$ : including all driving terms (top panel); excluding the drift-waves drive (middle panel); excluding the ballooning drive (bottom panel).

curvature operator by assuming a circular tokamak geometry, motivated by the fact that in the stellarator simulated in this work, the magnitude of the magnetic field varies, up to first order, with  $1/R$ . After linearizing the equations and evaluating the curvature operator at the low-field side, the study of the linear modes reduces to an eigenvalue equation. In figure 6 (top panel), we show the eigenmode solution with  $m = 4$  and  $n = 5$ , corresponding to the wavenumbers of the coherent mode observed in the nonlinear simulation. Similarly to the perturbation appearing in the non-linear simulation, the linear mode is large close to the LCFS and its amplitude decreases towards the core.

We now show that the identified linear mode is able to transport the radial  $E \times B$ -flux of the non-linear simulation. For this purpose, we consider the  $E \times B$ -flux as given by equation (9) for the linear eigenmode. The phase difference is obtained simply by computing the phase between the density and potential eigenfunctions of the mode. We determine the amplitude of the linear mode from a balance between the radial  $E \times B$ -flux and the plasma source:

$$\int_{\partial\Omega} \Gamma^c dS = \int_{\Omega} S_n \rho_* dV, \quad (11)$$

where  $\Omega$  is the volume contained inside the LCFS and  $\partial\Omega$  its surface area. Using equations (9) and (11) we obtain

$$|\tilde{n}\tilde{\phi}| \sim \frac{2B}{k_y} \frac{\int_{\Omega} S_n \rho_* dV}{\int_{\partial\Omega} dS} \frac{1}{\sin(\delta_{\Phi-n})}. \quad (12)$$

While for most  $(m, n)$  modes the amplitude of the perturbations obtained from equation (12) exceeds by orders of magnitude the one observed in the non-linear simulation, for the  $m = 4$ ,

$n = 5$  mode we obtain  $|\tilde{n}\tilde{\phi}| \sim 0.4$ , which is comparable to the values observed in the non-linear simulation (see figure 5).

Finally, we address the nature of the  $m = 4$  mode by removing either the ballooning or the drift-waves instabilities from the linear equations. The drive of the former is removed by zeroing out the curvature term of the vorticity equation, equation (6). On the other hand, by removing the parallel gradient terms of temperature and pressure in Ohm's law, equation (4), we preclude drift-waves from the system. As shown in figure 6, the eigenmode is not significantly affected by the removal of the drift-waves (middle panel). On the other hand, the eigenmode without ballooning drive (bottom panel) is significantly different and is no longer localized in the edge region. Thus, the linear theory points to a ballooning-like nature of the mode that dominates the simulation, a finding to be confirmed by linear analysis that take into account a more complex geometry.

To conclude, the GBS code has been upgraded to simulate plasma turbulence in three-dimensional magnetic configurations such as those of stellarators, but also of tokamaks with 3D perturbations. This letter presents the first global fluid simulation of the plasma dynamics in a stellarator with an island divertor. We show that, in the particular configuration produced with the Dommashck potentials considered here, the dynamics of the plasma is dominated by a coherent low ( $m = 4$ ) poloidal mode, with no blobs detaching into the SOL. The mode is studied with a non-local linear model, which points out the ballooning-like nature of this mode. These results highly contrast with typical tokamak boundary simulations and investigations are ongoing to understand the cause of this difference, as well as the link with experimental observations.

## Acknowledgments

The authors thank Per Helander and Brendan Shanahan for useful discussions. The simulations presented herein were carried out in part at the Swiss National Supercomputing Centre (CSCS) under the projects ID s1118 and s1126, and in part on the CINECA Marconi supercomputer under the GBSS-TEL and TSVV3 projects. This work, supported in part by the Swiss National Science Foundation, has been carried out within the framework of the EUROfusion Consortium and has received funding from the Euratom research and training programme 2014–2018 and 2019–2020 under Grant Agreement No. 633053. The views and opinions expressed herein do not necessarily reflect those of the European Commission.

## ORCID iDs

A.J. Coelho  <https://orcid.org/0000-0002-8889-7259>

M. Giacomin  <https://orcid.org/0000-0003-2821-2008>

## References

- [1] Loarte A. *et al* 2007 Progress in the ITER Physics Basis Chapter 4: Power and particle control *Nucl. Fusion* **47** S203
- [2] Reimerdes H. *et al* 2020 Assessment of alternative divertor configurations as an exhaust solution for DEMO *Nucl. Fusion* **60** 066030
- [3] Faitsch M., Sieglin B., Eich T., Herrmann A. and Suttrop W. 2017 Divertor heat load in ASDEX Upgrade L-mode in presence of external magnetic perturbation *Plasma Phys. Control. Fusion* **59** 095006
- [4] Kim K. *et al* 2017 Comparison of divertor heat flux splitting by 3D fields with field line tracing simulation in KSTAR *Phys. Plasmas* **24** 052506
- [5] Pedersen T.S. *et al* 2019 First results from divertor operation in Wendelstein 7-X *Plasma Phys. Control. Fusion* **61** 014035
- [6] Ohya N. *et al* 1984 The large helical device (LHD) helical divertor *Nucl. Fusion* **34** 387
- [7] Bader A., Boozer A.H., Hegna C.C., Lazerson S.A. and Schmitt J.C. 2017 HSX as an example of a resilient non-resonant divertor *Phys. Plasmas* **24** 032506
- [8] Ricci P. and Rogers B.N. 2013 Plasma turbulence in the scrape-off layer of tokamak devices *Phys. Plasmas* **20** 010702
- [9] Zweben S.J., Boedo J.A., Grulke O., Hidalgo C., LaBombard B., Maqueda R.J., Scarin P. and Terry J.L. 2007 Edge turbulence measurements in toroidal fusion devices *Plasma Phys. Control. Fusion* **49** S1
- [10] Happel T., Greiner F., Mahdizadeh N., Nold B., Ramisch M. and Stroth U. 2009 Generation of intermittent turbulent events at the transition from closed to open field lines in a toroidal plasma *Phys. Rev. Lett.* **102** 255001
- [11] Birkenmeier G. *et al* 2011 Experimental investigation of the magnetic configuration dependence of turbulent transport *Phys. Rev. Lett.* **107** 255001
- [12] Fuchert G., Birkenmeier G., Ramisch M. and Stroth U. 2016 Characterization of the blob generation region and blobby transport in a stellarator *Plasma Phys. Control. Fusion* **58** 054005
- [13] Zoletnik S. *et al* 2020 Multi-diagnostic analysis of plasma filaments in the island divertor *Plasma Phys. Control. Fusion* **62** 014017
- [14] Killer C., Shanahan B., Grulke O., Endler M., Hammond K. and Rudischhauser L. 2020 Plasma filaments in the scrape-off layer of Wendelstein 7-X *Plasma Phys. Control. Fusion* **62** 085003
- [15] Killer C., Narbutt Y. and Grulke O. (the W7-X Team) 2021 Turbulent transport in the scrape-off layer of Wendelstein 7-X *Nucl. Fusion* **61** 096038
- [16] Tanaka H., Masuzaki S., Ohno N., Morisaki T. and Tsuji Y. 2013 Intermittent transport in edge plasma with a 3D magnetic geometry in the large helical device *J. Nucl. Mater.* **438** S563
- [17] Tanaka H., Masuzaki S., Ohno N., Morisaki T. and Tsuji Y. 2015 Multi-pin Langmuir probe measurement for identification of blob propagation characteristics in the large helical device *J. Nucl. Mater.* **463** 761
- [18] Tsui C.K. *et al* 2018 Filamentary velocity scaling validation in the TCV tokamak *Phys. Plasmas* **25** 072506
- [19] Zweben S.J. *et al* 2016 Blob structure and motion in the edge and SOL of NSTX *Plasma Phys. Control. Fusion* **58** 044007
- [20] Shanahan B. and Huslage P. 2020 Filament simulations in regions of highly-varying parallel connection length *J. Plasma Phys.* **86** 905860314
- [21] Shanahan B., Dudson B. and Hill P. 2019 Fluid simulations of plasma filaments in stellarator geometries with BSTING *Plasma Phys. Control. Fusion* **61** 025007
- [22] Ricci P., Halpern F.D., Jolliet S., Loizu J., Masetto A., Fasoli A., Furno I. and Theiler C. 2012 Simulation of plasma turbulence in scrape-off layer conditions: the GBS code, simulation results and code validation *Plasma Phys. Control. Fusion* **54** 124047
- [23] Giacomin M. *et al* 2021 The GBS code for the self-consistent simulation of plasma turbulence and kinetic neutral dynamics in the tokamak boundary (arXiv:2112.03573)
- [24] Giacomin M., Stenger L.N. and Ricci P. 2020 Turbulence and flows in the plasma boundary of snowflake magnetic configurations *Nucl. Fusion* **60** 024001
- [25] Beadle C.F. and Ricci P. 2020 Understanding the turbulent mechanisms setting the density decay length in the tokamak scrape-off layer *J. Plasma Phys.* **86** 175860101
- [26] Giacomin M. and Ricci P. 2020 Investigation of turbulent transport regimes in the tokamak edge by using two-fluid simulations *J. Plasma Phys.* **86** 905860502
- [27] Mancini D., Ricci P., Vianello N., Giacomin M. and Corrado A. 2021 Investigation of the density shoulder formation by using self-consistent simulations of plasma turbulence and neutral kinetic dynamics *Nucl. Fusion* **61** 126029
- [28] Giacomin M., Stagni A., Ricci P., Boedo J.A., Horacek J., Reimerdes H. and Tsui C.K. 2021 Theory-based scaling laws of near and far scrape-off layer widths in single-null L-mode discharges *Nucl. Fusion* **61** 076002
- [29] Zeiler A. 1999 *Tokamak Edge Turbulence IPP 5/88* Max-Planck-Institut für Plasmaphysik
- [30] Krause N. *et al* 2002 The Torsatron TJ-K, an experiment for the investigation of turbulence in a toroidal low-temperature plasma *Rev. Sci. Instrum.* **73** 10
- [31] Loizu J., Ricci P., Halpern F.D. and Jolliet S. 2012 Boundary conditions for plasma fluid models at the magnetic presheath entrance *Phys. Plasmas* **19** 122307
- [32] Masetto A., Halpern F.D., Jolliet S., Loizu J. and Ricci P. 2015 Finite ion temperature effects on scrape-off layer turbulence *Phys. Plasmas* **22** 012308
- [33] Paruta P., Ricci P., Riva F., Wersal C., Beadle C. and Frei B. 2018 Simulation of plasma turbulence in the periphery of diverted tokamak by using the GBS code *Phys. Plasmas* **25** 012301

- [34] Dommaschk W. 1986 Representations for vacuum potentials in stellarators *Comput. Phys. Commun.* **40** 203
- [35] Braun S. and Helander P. 2010 Pfirsch–Schlüter impurity transport in stellarators *Phys. Plasmas* **17** 072514
- [36] Paruta P., Beadle C., Ricci P. and Theiler C. 2019 Blob velocity scaling in diverted tokamaks: a comparison between theory and simulation *Phys. Plasmas* **26** 032302
- [37] Shanahan B.W. and Dudson B.D. 2016 Blob dynamics in TORPEX poloidal null configurations *Plasma Phys. Control. Fusion* **58** 125003